Computer Physics Communications 305 (2024) 109349

Contents lists available at ScienceDirect

Computer Physics Communications

journal homepage: www.elsevier.com/locate/cpc

Computational Physics

QRCODE: Massively parallelized real-time time-dependent density functional theory for periodic systems

Min Choi [a], Mahmut Sait Okyay [a], Adrian Perez Dieguez [b], Mauro Del Ben [b], Khaled Z. Ibrahim [b], Bryan M. Wong [a,*]

[a] Department of Chemistry, Department of Physics & Astronomy, and Materials Science & Engineering Program, University of California-Riverside, Riverside, California 92521, USA

[b] Applied Mathematics & Computational Research Division, Lawrence Berkeley National Laboratory, Berkeley, California 94720, USA

ARTICLE INFO

The review of this paper was arranged by Prof. Blum Volker

Keywords:
Real-time time-dependent density functional theory
Massive parallelization
Periodic systems
Electron dynamics
Quantum dynamics
Harmonic generation

ABSTRACT

We present a new software module, QRCODE (Quantum Research for Calculating Optically Driven Excitations), for massively parallelized real-time time-dependent density functional theory (RT-TDDFT) calculations of periodic systems in the open-source Qbox software package. Our approach utilizes a custom implementation of a fast Fourier transformation scheme that significantly reduces inter-node message passing interface (MPI) communication of the major computational kernel and shows impressive scaling up to 16,344 CPU cores. In addition to improving computational performance, QRCODE contains a suite of various time propagators for accurate RT-TDDFT calculations. As benchmark applications of QRCODE, we calculate the current density and optical absorption spectra of hexagonal boron nitride (h-BN) and photo-driven reaction dynamics of the ozone-oxygen reaction. We also calculate the second and higher harmonic generation of monolayer and multi-layer boron nitride structures as examples of large material systems. Our optimized implementation of RT-TDDFT in QRCODE enables large-scale calculations of real-time electron dynamics of chemical and material systems with enhanced computational performance and impressive scaling across several thousand CPU cores.

1. Introduction

Electron dynamics calculations play a crucial role in probing light-matter interactions [1-3], photocatalytic reactions [4], and topological properties in solid-state materials [5-9]. In particular, the electric current or polarization response of materials to incident light has provided critical insight into several fundamental concepts, such as time-dependent perturbation theory [10,11], photogalvanic effects [5,10,12-14], topologically protected responses [6,8,15], nonlinear optics [16,17], and harmonic generation [18,19]. Among the various theoretical approaches for simulating electron dynamics in materials, [20-24] time-dependent density functional theory (TDDFT) is one of the most widely used due to its accuracy and computational cost balance [25-27]. TDDFT is divided into two major categories: (i) linear-response TDDFT (LR-TDDFT) where time-dependent perturbation theory is used to estimate material responses in the frequency domain [28-34], and (ii) real-time TDDFT (RT-TDDFT), which explicitly evolves the wavefunction in real-time by iteratively solving the time-dependent Schrödinger equation [35-45]. Real-space approaches [46-49], such as atomic orbital basis sets or finite-difference methods, are well-suited for molecular systems. However, the use of plane-wave basis sets is more appropriate for analyzing the real-time dynamics of periodic systems, such as crystal structures, metals, and semiconductors. Moreover, plane-wave basis sets can be systematically improved by increasing the energy cutoff, in contrast to atomic orbital basis sets, which can incur linear dependence problems in periodic systems. The resulting electron dynamics in the RT-TDDFT scheme are obtained by time-propagation of the Kohn-Sham (KS) wavefunctions $|\psi_{n,\vec{k}}(t)\rangle$ via the time-dependent Kohn-Sham (TDKS) equation,

$$i\hbar\frac{\partial}{\partial t}\left|\psi_{n,\vec{k}}(t)\right\rangle = \widehat{H}_{\mathrm{KS}}(t)\left|\psi_{n,\vec{k}}(t)\right\rangle \tag{1}$$

The time-dependent Kohn-Sham Hamiltonian, $\widehat{H}_{KS}(t)$, is given as

$$\widehat{H}_{\mathrm{KS}}(t) = \widehat{T}(t) + \widehat{V}_{\mathrm{ext}}(t) + \widehat{V}_{\mathrm{HXC}}[\rho(t)] \tag{2}$$

* Corresponding author.
E-mail address: bryan.wong@ucr.edu (B.M. Wong).

https://doi.org/10.1016/j.cpc.2024.109349
Received 28 March 2024; Received in revised form 18 July 2024; Accepted 13 August 2024
Available online 14 August 2024

where $\widehat{T}$, $\widehat{V}_{\text{ext}}$, and $\widehat{V}_{\text{HXC}}$ are the kinetic energy, external ionic potential, and Hartree-exchange-correlation potential, respectively, which is a functional of the time-dependent charge density, $\rho(t) = \sum_{n,\vec{k}} |\psi_{n,\vec{k}}(t)|^2$.

While there are a few RT-TDDFT software programs for condensed matter applications, such as TDAP [26,46-48], INQ [50], Salmon [51], Elk [52], and OCTOPUS [53-56], our implementation introduces several optimizations that enhance computational efficiency and scalability for large systems.

Large-scale electron dynamics calculations are essential for probing electronic-excited phenomena in realistic systems, such as photo-induced reactivity of materials with defects [57,58] or interlayer electron transfer in heterostructures [59,60]. Of the various electronic excited-state methods used to probe material systems at the atomistic level, RT-TDDFT with plane-wave basis sets is one of the most promising approaches due to its favorable balance between accuracy and computational cost. To this end, we have developed a new software module, QRCODE (Quantum Research for Calculating Optically Driven Excitations), for massively parallelized RT-TDDFT calculations of large-scale periodic systems in the open-source Qbox software package [61-64]. QRCODE introduces new command line parameters for enhanced parallelization and Ehrenfest dynamics for coupled electron-ion simulations. In particular, QRCODE contains a massively parallel FFT scheme (OPT-FFT) for efficient RT-TDDFT calculations of periodic material systems built on top of the latest version of Qbox (Version 1.76.1), which includes significant bug fixes. Our implementation is a separate and independent development from the QB@LL code [65-67], and QRCODE offers unique features and optimizations tailored to the latest Qbox framework. We perform four case studies to benchmark and validate our RT-TDDFT implementation: Ehrenfest dynamics for an H_2 molecule, electronic-excited ozone-oxygen cycle reactions, absorption spectra, and high harmonic generation in stacked layers of hexagonal boron nitride (h-BN). Finally, we conclude with possible future developments and applications of QRCODE.

2. Theoretical background and methodology

2.1. Optimization of the parallel FFT implementation for RT-TDDFT calculations

The Qbox software package uses MPI parallelization schemes for memory and task distribution of plane-wave wavefunctions. For a given spin state of a k-point in the Brillouin zone, each MPI process is assigned with an array of size nst_loc × ngw_loc, where nst_loc (ngw_loc) is the number of states (G-vectors) divided by the number of the state (G-vector) parallelization blocks set by the user during job submission. Together with the wavefunctions and states, parallelization of spin indices and k-points gives rise to a four-dimensional communicator of dimensions [64]. The plane-wave-based Qbox code executes the Hamiltonian-wavefunction multiplication in Fourier space to construct the Hamiltonian matrix elements, and the distributed wavefunction data is collected by the MPI_Alltoallv operation during the execution of 3D fast Fourier transformations (FFTs). Each time this operation is required, the computation is parallelized across the assigned MPI ranks, where forward and backward 3D-FFTs are applied to each wavefunction in a distributed fashion, together with some linear algebra operations on the corresponding vectors.

As depicted in Fig. 1(a), profiling the overall execution with the existing Qbox code using the Cray PAT profiler showed a critical communication bottleneck in calculating the distributed 3D-FFT operation for each state by the MPI_Alltoallv routine. This numerical approach is especially critical when many MPI ranks are involved, and each MPI rank participates in the computation of the assigned local state. The MPI ranks for allocated G-vector blocks work together to calculate the FFT of each state and repeat this process for their nst_loc

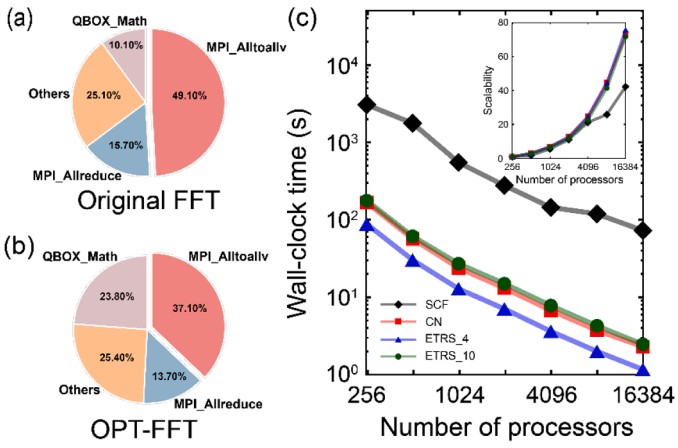

Fig. 1. Computational performance tests. Wall-clock time analysis of the (a) original FFT and (b) OPT-FFT implementations for the time-evolution of a magnesium porphyrin molecule comprised of 37 atoms: one magnesium, 20 carbon, 4 nitrogen, and 12 hydrogen atoms with a 40 Ry energy cutoff. (c) Wall-clock time of the self-consistent procedure in the original Qbox code (SCF), CN, and ETRS time propagators for a 4 × 4 h-BN supercell with a 6 × 6 × 1 k-sampling and a 40 Ry cutoff energy. The inset in (c) represents the scalability of the same routines. For the ETRS method, the 4th- (ETRS_4) and 10th-order (ETRS_10) Taylor expansions are profiled. The runtime of each approach is averaged by the total number (30) of executed iterations. The most efficient parallelization configuration was selected for each number of processors, namely 252, 504, 1008, 2016, 4068, 8172, and 16,344. We employed the PBE functional [81] with ONCV norm-conserving pseudopotentials [71] for our performance test calculations.

local states. For each state and rank, the overall computation is decomposed into four steps: (1) mapping and padding local data from a sphere band to a cube layout, (2) performing a 2D-FFT on local data, (3) packing local data and performing MPI_Alltoallv for transposing the global cube-structure among the participating ranks, and (4) performing a 1D-FFT on the transposed local data. The order and inversion of these steps depend on the FFT direction being calculated, but every rank must repeat them nst_loc times in each forward and backward direction. Additionally, the FFT is called several times during the SCF convergence iterations, and, therefore, the MPI_Alltoallv operation significantly impacts global performance. Additional methodological details and graphical insights on the parallelization and optimization process are provided in Section 1 of the Supplementary Material.

Since the computation of the wavefunctions is independent, QRCODE contains an optimized version of the FFT routine where only one MPI_Alltoallv operation is executed instead of nst_loc communications. By keeping the G-vectors parallelized, each MPI process stores the data to be transposed for each state contiguously in the memory buffer. After completing the previous FFT steps for all states, the MPI communication on this buffer is performed only once. This optimization leads to the following performance gains:

(1) Overhead reduction: MPI routines have an intrinsic overhead, such as initialization, data copying, and synchronization. This overhead is reduced by performing a single MPI routine on a large data buffer. The communication pattern is also potentially optimized by executing a single MPI routine on a large data buffer.
(2) Load balancing: By performing a single MPI routine on a large data buffer, better load balancing can be achieved by splitting the data into smaller chunks, which can be challenging to balance across all the MPI processes.
(3) Cache utilization: More data is kept in the cache, which can improve its utilization and lead to better performance.

2.2. Time propagator

We implemented the enforced time-reversal symmetry (ETRS) [68] and Crank-Nicolson (CN) [69] time propagation algorithms in QRCODE to evolve the KS wavefunctions for our RT-TDDFT simulations. The ETRS method is based on time-reversal symmetry as follows:

$$\exp\Big(-i\frac{\Delta t}{2}\widehat{H}_{\mathrm{KS}}(t)\Big)\psi_{n,\vec{k}}(t)=\exp\Big(i\frac{\Delta t}{2}\widehat{H}_{\mathrm{KS}}(t+\Delta t)\Big)\psi_{n,\vec{k}}(t+\Delta t), \tag{3}$$

where Δt indicates the time step for propagation. The left-hand side of Eq. (3) propagates the KS wavefunction from t to $t+\Delta t/2$, whereas the right-hand side propagates it from $t+\Delta t$ to $t+\Delta t/2$. The exponential terms can be expressed as an Nth-order Taylor expansion $\exp(\widehat{A})=\sum_{n=1}^{N}\frac{\widehat{A}^n}{n!}+\mathrm{erf}(\widehat{A})$. The KS Hamiltonian in the next time step, $\widehat{H}_{\mathrm{KS}}(t+\Delta t)$, is iteratively updated using the KS wavefunction, $\psi_{n,\vec{k}}(t+\Delta t)$, until Eq. (3) is satisfied.

The KS wavefunction can be propagated through a midpoint scheme [68] using the CN algorithm, which is based on the first-order expansion of the ETRS expression. The algorithm in the midpoint approximation preserves the unitarity of the operator. The KS wavefunction in the CN algorithm at time $t+\Delta t$ is obtained by solving the following linear matrix equation:

$$\Big[1-i\frac{\Delta t}{2}\widehat{H}_{\mathrm{KS}}\Big(t+\frac{\Delta t}{2}\Big)\Big]\psi_{n,\vec{k}}(t)=\Big[1+i\frac{\Delta t}{2}\widehat{H}_{\mathrm{KS}}\Big(t+\frac{\Delta t}{2}\Big)\Big]\psi_{n,\vec{k}}(t+\Delta t), \tag{4}$$

where the midpoint Hamiltonian is defined as $\widehat{H}_{\mathrm{KS}}(t+\Delta t/2)=\widehat{H}_{\mathrm{KS}}[\rho(t+\Delta t/2)]$ with the midpoint density $\rho(t+\Delta t/2)\approx[\rho(t+\Delta t)+\rho(t)]/2$. We employed a conjugate gradient square algorithm [70] to solve this unitary linear matrix equation and obtain the KS wavefunctions. Subsequently, $\rho(t+\Delta t)$ and $\widehat{H}_{\mathrm{KS}}(t+\Delta t/2)$ are updated until Eq. (4) is satisfied self-consistently.

We performed convergence tests for the CN and various Taylor expansions of the ETRS time propagators (see Section 2 in the Supplementary Material). We used the CN time propagator for our Ehrenfest dynamics on the H_2 molecule and ozone-oxygen cycle examples in this work. We adopted the 6th-order ETRS and CN time propagators for the optical spectra for monolayer h-BN, the CN propagator for high harmonic generation simulations, and the 4th-order ETRS time propagator for multi-layer h-BN.

2.3. Velocity gauge

The time-dependent Kohn-Sham equation in the velocity gauge is given by

$$i\hbar\frac{\partial}{\partial t}\Big|\psi_{n,\vec{k}}(t)\Big\rangle=\Big[\frac{1}{2m}\Big(-i\hbar\vec{\nabla}+\frac{e}{c}\vec{A}(t)\Big)+\vec{V}_{\mathrm{ext}}(\vec{r})+\widehat{V}_{\mathrm{HXC}}[\rho(\vec{r},t)]\Big]\Big|\psi_{n,\vec{k}}(t)\Big\rangle \tag{5}$$

where $\vec{A}(t)$ is the external vector potential of the form $\vec{A}(t)=-c\int_0^t\vec{E}(\tau)d\tau$. From the velocity gauge, we can obtain the current density as follows:

$$J(t)=-\frac{e}{m}\sum_{n,\vec{k}}\frac{f_{n,\vec{k}}}{S}\Big\langle\psi_{n,\vec{k}}(t)\Big|\widehat{\vec{\pi}}(t)\Big|\psi_{n,\vec{k}}(t)\Big\rangle \tag{6}$$

where $\widehat{\vec{\pi}}(t)=\frac{m}{i\hbar}[\widehat{\vec{r}},\widehat{H}]=\widehat{\vec{p}}+\frac{e}{c}\vec{A}+\frac{im}{\hbar}[\widehat{V}_{\mathrm{NL}},\vec{r}]$ is the quantum mechanical momentum operator, $f_{n,\vec{k}}$ is the occupation factor of the nth state with momentum $\vec{k}$, and S is the surface area perpendicular to the current flow direction. The velocity operator $\frac{1}{i\hbar}[\widehat{\vec{r}},\widehat{H}]$ contains a contribution from the ionic potential because of the nonlocality of the pseudopotential, $\widehat{V}_{\mathrm{NL}}$, which does not commute with the position operator. The commutator between the nonlocal pseudopotential and position operator can be obtained from the nonlocal current density, which we obtain from the expression

$$\Big\langle\psi_{n,\vec{k}}(t)\Big|\frac{im}{\hbar}[\widehat{V}_{\mathrm{NL}},\vec{r}]\Big|\psi_{n,\vec{k}}(t)\Big\rangle=\frac{im}{\hbar}\Big[\Big\langle\psi_{n,\vec{k}}(t)\Big|\widehat{V}_{\mathrm{NL}}\vec{r}\Big|\psi_{n,\vec{k}}(t)\Big\rangle-\Big\langle\psi_{n,\vec{k}}(t)\Big|\vec{r}\widehat{V}_{\mathrm{NL}}\Big|\psi_{n,\vec{k}}(t)\Big\rangle\Big]. \tag{7}$$

The first part of the nonlocal current density can be calculated with the expression

$$\Big\langle\psi_{n,\vec{k}}(t)|\widehat{V}_{\mathrm{NL}}\vec{r}|\psi_{n,\vec{k}}(t)\Big\rangle=\langle\psi_{n,\vec{k}}(t)|\widehat{V}_{\mathrm{NL}}\mathrm{FT}\Big[\vec{r}\,\mathrm{IFT}\Big[|\psi_{n,\vec{k}}(t)\rangle\Big]\Big], \tag{8}$$

where FT and IFT denote the Fourier transform and inverse Fourier transform, respectively. In the same manner, the last term can also be calculated with the expression

$$\Big\langle\psi_{n,\vec{k}}(t)\Big|\vec{r}\widehat{V}_{\mathrm{NL}}\Big|\psi_{n,\vec{k}}(t)\Big\rangle=\langle\psi_{n,\vec{k}}(t)|\mathrm{FT}\Big[\vec{r}\widehat{V}_{\mathrm{NL}}\mathrm{IFT}\Big[|\psi_{n,\vec{k}}(t)\rangle\Big]\Big]. \tag{9}$$

One can extract the permittivity tensor from the real-time current density with

$$\varepsilon_{ij}(\omega)=1+\frac{4\pi i\sigma_{ij}(\omega)}{\omega} \tag{10}$$

where ω is the frequency of the applied field and $\sigma_{ij}(\omega)=\frac{\mathrm{FT}\big[\vec{J}_j(t)\big]}{\mathrm{FT}\big[\vec{E}_i(t)\big]}$ is the optical conductivity.

2.4. Ehrenfest dynamics

To simulate electron-ion coupled dynamics beyond the Born-Oppenheimer approximation, the ionic forces must be computed in real time from the dynamic potential energy surface. While this mean-field-based single-body approach is useful for simulating the dynamics of an excited-state electron-ion coupled system, it is worth noting that it cannot capture multireference electronic structure effects. The forces acting on each ion can be calculated by differentiation of the energy surface, which itself is dependent on the time-dependent charge density. These forces are given by:

$$M_I\frac{d^2\vec{R}_I(t)}{dt^2}=-\nabla_{\vec{R}_I}\sum_{n,\vec{k}}\Big\langle\psi_{n,\vec{k}}(\vec{r},t)\Big|\widehat{H}_{\mathrm{KS}}[\rho(\vec{r},t)]\Big|\psi_{n,\vec{k}}(\vec{r},t)\Big\rangle, \tag{11}$$

where M_I and $\vec{R}_I$ are the mass and position, respectively, of the Ith atom [36]. As the charge density is not in an adiabatic state, the forces calculated through this theorem differ from those derived under the Born-Oppenheimer ground state framework. Accordingly, the dynamics obtained by this approach are commonly referred to as Ehrenfest dynamics [71].

2.5. Second- and high-harmonic generation (SHG and HHG)

Harmonic generations are fundamental nonlinear optical processes in which the material responds with an integer-multiple frequency of the applied driving field [72]. While the most commonly studied effect is second-harmonic generation (SHG), which is the response of a material with a doubled frequency, high-harmonic generation (HHG) has also gathered substantial interest in material characterization and symmetry analysis [73-75]. In computational material science, calculating SHG

and HHG signals provides a stringent test to determine the reliability and accuracy of first-principles computational codes.

For a 2D insulator, the SHG results obtained by RT-TDDFT calculations can be compared with the SHG polarization susceptibility tensor in the sub-bandgap regime,

$$\mathrm{Im}[\chi^{yxx}(-2\omega;\omega,\omega)] = \frac{8\pi e^3}{\hbar^2}\int_{\vec{k}} \mathrm{Im}\sum_{nmp}\frac{f_{n,\vec{k}}\left(1-f_{n,\vec{k}}\right)\nu^{y}_{nm}\nu^{x}_{mp}\nu^{x}_{pn}}{\omega^{3}_{mn}\left(\omega_{mp}+\omega_{np}\right)}\delta(2\omega-\omega_{mn}) \quad (12)$$

where $\omega_{mn} = \left(\varepsilon_{m,\vec{k}} - \varepsilon_{n,\vec{k}}\right)/\hbar$ is the ground state energy difference between eigenstates $|\psi_{m,\vec{k}}\rangle$ and $|\psi_{n,\vec{k}}\rangle$, ν^{α}_{nm} are the Cartesian components of the dipole matrix element $\left\langle \psi_{n,\vec{k}}\middle|\widehat{\vec{\pi}}\middle|\psi_{m,\vec{k}}\right\rangle$, and $\int_{\vec{k}} = \int \frac{d^2\vec{k}}{4\pi^2}$ denotes a 2D Brillouin zone integration.

3. Results and discussion

3.1. Performance tests

The FFT calculations in QRCODE are optimized by reducing the number of MPI_Alltoallv calls required per rank. Instead of consecutively completing the 4-step FFT calculation for each band, we grouped the steps for all bands. First, the mapping-and-padding and 2D-FFT steps are completed for nst_loc bands. Before the packing-and-transposing step, we allocate larger sending-buffer and receiving-buffer sizes to store the data of the nst_loc bands together. We then pack data of the different bands that will be sent to the same rank. Lastly, the 1D-FFT step is performed for all local bands, modifying the access indexing when unpacking the data from the communication collective. This process creates larger buffer memories, transferring more data than the original Qbox implementation. However, only one call to MPI_Alltoallv is required instead of nst_loc times, which decreases the overhead in communication by a factor of nst_loc. The QRCODE calculations were carried out on the Perlmutter supercomputer at NERSC [76], which is currently comprised of 3,072 CPU-only and 1,534 GPU-accelerated nodes. In our performance test, we used nodes composed of one AMD EPYC 7763 (Milan) CPU with 64 cores with 2 threads per CPU. Each node has 256 GB of DDR4 DRAM, achieving 204 GB/s CPU memory bandwidth. Each node has four HPE Slingshot 11 NIC (4 × 25GB/s) to interconnect nodes. Therefore, the 16,344 MPI tasks correspond to 128 nodes (with 128 tasks each). We utilized all available cores/threads by assigning them as MPI ranks without distributing the workload using OpenMP parallelization. We used the -O3 flag for building Qbox with the GNU GCC 11.2.0 version. For the linked libraries, we used the FFTW Cray implementation and the LibSci Cray library [77], which comprises a tuned Cray implementation for BLAS [78], LAPACK [79], and ScaLAPACK, available in Perlmutter, and the Xerces-C++ XML parser version 3.2.4 [80].

As seen in Figs. 1(a) and 1(b), the overall wall-clock portion of the MPI_Alltoallv operation for 100 RT-TDDFT time-propagation steps of a magnesium porphyrin molecule is reduced from 49.1% to 37.1% when utilizing the OPT-FFT routine. Most importantly, the overall execution time of the computation also decreased by 23%. The system is comprised of 64 states and is parallelized by 128 processors in the G-vector dimension. Note that the effect of the OPT-FFT routine in the overall run time is particularly significant when the state and G-vector dimensions are massively parallelized since the amount of data transferred per MPI rank in each MPI_Alltoallv becomes smaller. A detailed comparison of wall-clock times between the original FFT and OPT-FFT implementations is described in Section 4 of the Supplementary Material.

The SCF routine is a time-independent step in our workflow and is called once to obtain the ground KS wavefunction before the RT-TDDFT iterations. As it starts with a guess density to be optimized, the SCF routine takes much longer than each individual step of the CN and ETRS time propagators (Fig. 1(c)). The most salient result of Fig. 1(c) is the parallelizability of our RT-TDDFT implementation in QRCODE, which shows impressive scaling on up to 16,344 CPUs. To determine the optimal distribution of nspb, nkpb, nstb, and ngb MPI tasks, various parallelization configurations were tested, and the most efficient configuration was used to calculate the wall-clock time (see Section 3 in the Supplementary Material). It is also worth noting that interference of concurrently running jobs in the system can lead to runtime variations, and no two executions of the same parallel program using the same input will finish execution precisely with the same run time. Therefore, we took the average runtime of each time propagator over the total number of executed iterations to minimize this runtime variability. However, as the SCF routine is completed only once, minor variations can be observed in its scalability factor across different executions that execute the same SCF step on the same data. As shown in Fig. 1(c), the time propagator and its order play a crucial role in the wall-clock time. However, the efficiency becomes similar regardless of the type or order of time propagator, as demonstrated in the scalability plot, inset in Fig. 1 (c). Consequently, even when the time propagator is changed based on the system size or time step, the computational efficiency does not change significantly, allowing flexibility to select an appropriate time propagator for the system under study.

3.2. Ehrenfest dynamics of H_2

We used a simple hydrogen molecule model as a representative example to benchmark the Ehrenfest dynamics routines in QRCODE. Hydrogen is a molecule with a bond order of 1 with two electrons in a σ molecular orbital, which forms the bonding state. When one electron in the σ orbital is excited to the anti-bonding state (σ*), the molecule detaches into two hydrogen atoms with non-bonding electrons in each atomic 1s orbital [82,83]. Fig. 2 depicts this dissociative process with Ehrenfest dynamics computed with QRCODE. Two hydrogen atoms are

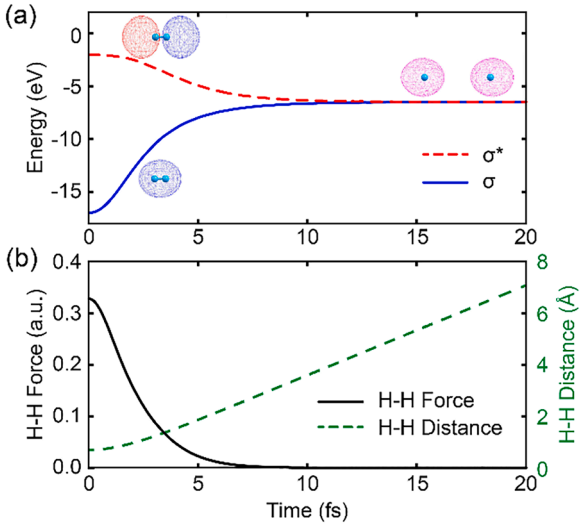

Fig. 2. Ehrenfest dynamics of an electronic-excited hydrogen molecule. Real-time dynamics of (a) energy eigenvalues, (b) force and distance between two hydrogen atoms after exciting an electron from a bonding to an anti-bonding state. The solid blue and dotted red lines in panel (a) indicate the energy of the bonding (σ) and anti-bonding (σ*) states, respectively. The sky-blue balls represent the hydrogen atoms, and the clouds surrounding the hydrogen atoms indicate the initial molecular and final atomic orbitals. The solid black and dotted green lines in panel (b) indicate the force and distance between the two hydrogen atoms.

initially separated by 0.693 Å and form σ bonding and σ* anti-bonding states. In the ground state, the occupations of the bonding and anti-bonding states are $f_\sigma = 2$ and $f_{\sigma^*} = 0$, respectively. We initiate this process by exciting an electron from the bonding to the anti-bonding state by artificially switching the occupation factors with $f_\sigma = f_{\sigma^*} = 1$ and propagate the electronic-excited system without any external perturbations. At the end of our simulation at 20 fs, the H–H distance elongates to 7 Å, and the eigenenergies of the molecular states converge to the atomic 1s state eigenvalue. The interatomic force drops to zero around 10 fs, indicating that the hydrogen atoms are completely non-interacting at that distance.

3.3. Ozone-oxygen reaction

As a more complex example of electronic-excited reaction dynamics to confirm our Ehrenfest dynamics implementation in QRCODE, we also simulated an ozone-oxygen reaction described by the following chemical reactions: [84]

$$O_3 + h\nu \rightarrow O_2 + O \quad (1)$$

$$O + O_2 \rightleftharpoons O_3 \quad (2)$$

$$O_3 + O \rightarrow 2O_2 \quad (3)$$

$$2O \rightarrow O_2 \quad (4)$$

We placed two ozone molecules in the center of a 3,375 $Å^3$ cubic supercell with a gamma point sampling and employed the PBE functional [81] with ONCV pseudopotentials [85]. As shown in Fig. 3, we initially excited electrons from two ozone molecules separated 2.59 Å apart to mimic reaction (1) and subsequently simulated Ehrenfest dynamics for 400 fs with a 2.42 as time step with the CN time propagator. Within 200 fs, the ozone molecules continuously vibrate and interconvert with each other as described in reaction (2). From 200 to 336 fs, the O2 and O5 atoms approach each other as they separate from their parent ozone molecules. Reactions (1), (2), and (3) occur simultaneously around 336 fs as the O1, O2, O4, and O5 atoms are nearly equidistant. After 336 fs, the O2 and O5 atoms bind to form an oxygen molecule, as defined in the reaction (4). As a result, three oxygen molecules are formed from the two electronic-excited ozone molecules.

3.4. Absorption spectrum of h-BN

To benchmark our RT-TDDFT velocity gauge implementation in QRCODE, we present the optical properties of monolayer hexagonal boron nitride (h-BN). We constructed the hexagonal unit cell of h-BN (a = 2.5124 Å) [86] with a 10.58 Å (20 Bohr) vacuum along the z-direction (Fig. 4(a)), a 40 Ry energy cutoff with a 12 × 12 × 1 Monkhorst pack k-point sampling, and employed the PBE functional [81] with ONCV pseudopotentials [85]. We applied a delta-kick perturbation [87,88] of 0.0001 Hartree and simulated the resulting RT-TDDFT dynamics with a 2.42 as time step. We obtained the real-time current density with the CN and ETRS (6th-order expansion) algorithms using Eq. (6). Both propagators exhibit the same response, as shown in Fig. 4(b). Moreover, the two absorption peaks near 6 eV due to the inter-band transition between the π to π^* bands observed in Fig. 4(c) are consistent with previous reports [89-91].

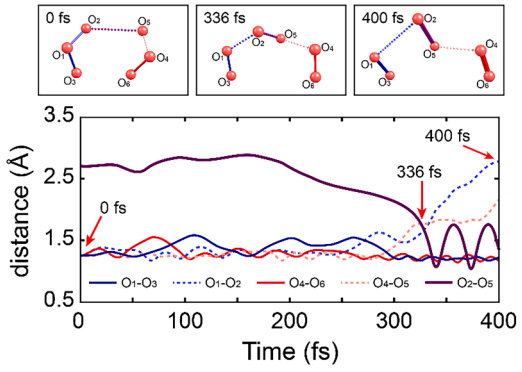

Fig. 3. Ehrenfest dynamics of the ozone-oxygen reaction. The lower panel depicts the distance between oxygen atom pairs during the electronic-excited reaction. The solid blue and orange lines denote the left and right ozone molecules at the initial time (0 fs). The purple line denotes the intermolecular distance between the O2 and O5 atoms, which separates the left and right ozone molecules that form the oxygen molecules. The solid and dotted lines represent the intramolecular and intermolecular distances of the final reaction products (400 fs). The geometries in the upper panel represent snapshots of the system at 0, 336, and 400 fs, as indicated by red arrows in the lower panel.

3.5. SHG and HHG in monolayer and multi-layer hBN

Finally, in this section, we analyze the nonlinear optical response of monolayer h-BN under various conditions to test the response sensitivity of our RT-TDDFT implementation in QRCODE. To enhance the accuracy for optical responses, we used a 24 × 24 × 1 k-point sampling and a 1.21 as timestep with the CN propagator. The inversion symmetry of a material must be broken to observe SHG and other even-order HHGs; [92, 93] therefore, the noncentrosymmetric nature of h-BN provides an excellent testbed to detect SHG and all orders of HHG [94].

We first explicitly calculate the SHG and HHG yields, as depicted in Fig. 5, by investigating the Fourier components of the transverse and longitudinal real-time current density response, $\vec{J}_\perp(t)$ and $\vec{J}_\parallel(t)$, in the x- and y-directions, respectively. We use a generic driving laser field, $\vec{E}(t) = E_0 e^{i\omega t}\hat{x}$, oscillating in the x-direction with a frequency at half the bandgap: $\omega = 2.32$ eV. We tested two different field strengths: 0.005 and 0.5 V/Å. The laser pulse field (Fig. 5(a)) is described by the vector potential $\vec{A}(t) = -\frac{e}{\omega}E_0 f(t)\sin(\omega t)\hat{x}$ with a polynomial envelope function given by:

$$f(t) = \begin{cases} 0, & t \le t_0 \\ 3(t/t_1)^2 - 2(t/t_1)^3, & t_0 < t \le t_1 \\ 1, & t_1 < t \le t_2 \\ 1 - 3[(t-t_2)/t_1]^2 - 2[(t-t_2)/t_1]^3, & t_2 < t \le t_2 + t_1 \\ 0, & t_2 + t_1 < t \end{cases}$$

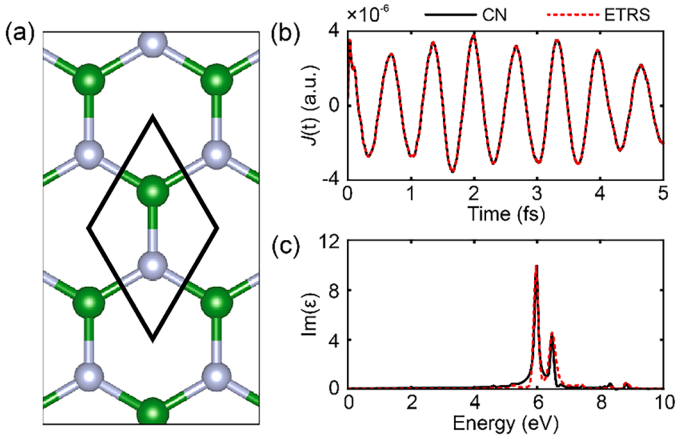

Fig. 4. Absorption spectrum of monolayer h-BN. (a) Geometrical structure of monolayer h-BN. The black parallelogram indicates the unit cell of h-BN. (b) Real-time current density and (c) absorption spectrum (imaginary part of the permittivity) calculated from Eq. (6) and (7). The solid black (dotted red) lines in (b) and (c) are obtained from the CN (ETRS) time-propagator.

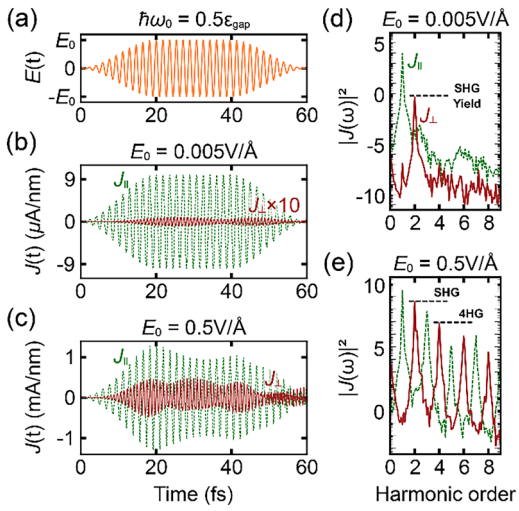

Fig. 5. Second and high-harmonic generation in monolayer h-BN. (a) Real-time profile of the *x*-polarized light pulse at a frequency of half the bandgap of h-BN. The brown (green) oscillating lines in (b) and (c) are the transverse (longitudinal) current density response of h-BN to the applied pulse with strengths $E_0 =$ 0.005 and 0.5 V/Å, respectively. The transverse response in (b) is scaled by 10 for visualization. Panels (d) and (e) are the Fourier transforms of the current densities in (b) and (c), respectively. The *x*-axis is scaled with the applied field frequency, and the *y*-axis is log-scaled. The horizontal dashed lines in panels (d) and (e) indicate the second and fourth-harmonic yields of the transverse response.

where $t_0 = 0$ fs, $t_1 = 20$ fs, and $t_2 = 40$ fs. The real-time current density response of h-BN within the 0 – 60 fs range for applied pulse strengths of 0.005 and 0.5 V/Å are shown in Figs. 5(b) and 5(c), respectively. The squared Fourier transforms, $|\vec{J}(\omega)|^2$, up to the eighth harmonic order of the applied field frequency, are shown in Figs. 5(d) and 5(e). The weaker field can induce only a longitudinal linear response and transverse SHG (Fig. 5(d)), while the stronger field produces several HHG signals (Fig. 5 (e)). Since h-BN preserves time-reversal symmetry, even-order HHGs are in the transverse direction, whereas linear response and odd-order HHGs are in the longitudinal direction for the *x*-polarized field, as expected [95]. Our QRCODE results are similar to previous reports obtained by RT-TDDFT calculations implemented in the Quantum Espresso package [86]. To provide a more quantitative analysis, we calculated the even-order Fourier components (SHG for the 2ω response component $\vec{J}^{2\omega}$, 4HG for the 4ω component $\vec{J}^{4\omega}$, etc.) and repeated the calculations for various conditions.

We examined the transverse SHG yields for various laser frequencies lower than the bandgap (Fig. 6(a)). These SHG yields can be studied in terms of the SHG susceptibility tensor given in Eq. (12). Fig. 6(a) shows the correspondence between the SHG current spectrum $\omega \times \mathrm{Im}[\chi^{yxx}(-2\omega;\omega,\omega)]$ (black solid line) and the SHG yields obtained from the real-time response (brown circles), even though the RT-TDDFT results are directly obtained without any perturbative approximation [86].

We now examine the polarization dependency of the SHG response by obtaining the longitudinal and transverse SHG yields for incident fields polarized in various directions with respect to the *x*-axis (Fig. 6 (b)). The obtained polarization anisotropy is consistent with the scientific literature [95,96]. Both transverse and longitudinal SHG yields give peaks every 60°, such that one is a maximum when the other is a minimum due to the 3-fold D_{3h} point group symmetry of monolayer h-BN. When the incident field is parallel to a vertical mirror plane, the transverse SHG response vanishes, and the longitudinal SHG response maximizes, resulting in alternating 6-fold anisotropy [95,97]. The maximum longitudinal response is around 0.67 of the maximum transverse response, which indicates that the transverse signals are more prominent in SHG spectroscopy.

The HHG yields for 0.001 - 1.0 V/Å field strengths are plotted in Fig. 6(c), where *n*HG denotes the *n*th-order HHG. It is worth noting that the SHG response is insignificant for weak fields below 0.001 V/Å. Similarly, the 4HG, 6HG, and 8HG peaks become noticeable when the field strength exceeds 0.03, 0.1, and 0.2 V/Å, respectively. The squared SHG yield follows the power law ($\propto E_0^4$) within the 0.002 - 0.3 V/Å range. However, under stronger fields, the slope deviates from the perturbative power law, which indicates that the system reaches the non-perturbative limit [74,86,95]. The results shown in Figs. 6(a) and 6(c) show better agreement with theoretical expectations compared to [Ref. 86], which was obtained by the Quantum Espresso package. Our results demonstrate that the RT-TDDFT formalism and implementation in QRCODE are suitable for a wide range of nonlinear optical response studies, particularly in the presence of strong fields.

To test our efficient implementation for large systems in QRCODE, we carried out RT-TDDFT calculations for a 4-layer h-BN structure separated by ~3.5 Å consisting of 56 atoms in the twisted $\sqrt{7} \times \sqrt{7}$ supercell (Fig. 7). We optimized the supercell of h-BN using the SCAN functional [98], which includes long-range interactions, with a 40 Ry energy cutoff and a $9 \times 9 \times 1$ Monkhorst pack *k*-point sampling; the PBE functional [81] with ONCV pseudopotentials [85] was used for the subsequent ground state and time propagation calculations. It is worth noting that this large RT-TDDFT simulation (60 fs (25,000 time steps) with 81 k-points parallelized into 81 ranks, ~22,000 G-vectors parallelized into 16 ranks, and 112 bands parallelized into 8 ranks, which used a total of 10,368 processors) took less than 15 hours on the *Perlmutter* supercomputer at NERSC. Moreover, the order of SHG yield

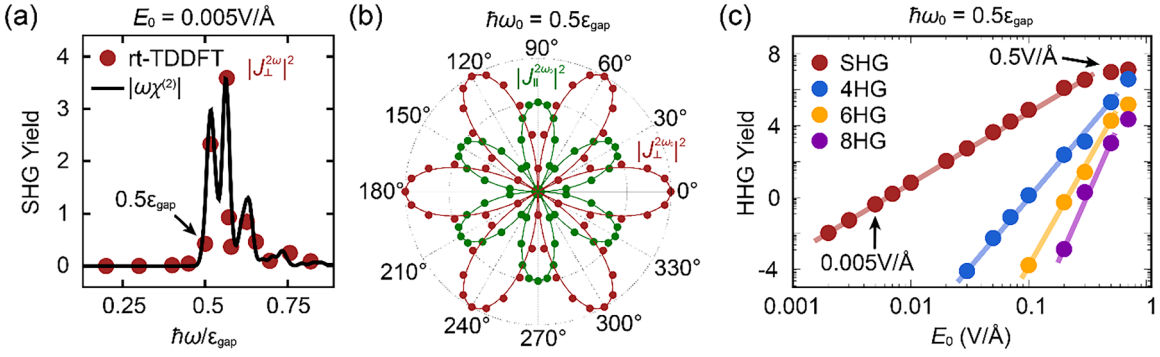

Fig. 6. Effect of field frequency, polarization, and strength on harmonic generation. (a) Theoretical SHG susceptibility spectrum of h-BN (black line) and the RT-TDDFT SHG yields (brown solid circles). (b) Polarization anisotropy of transverse (brown) and longitudinal (green) SHG yields. (c) SHG and HHG yields for various field strengths. Both axes are log scaled, and the arrows indicate the field strengths used in Fig. 5. The transparent brown, blue, yellow, and purple lines represent the square of the perturbative power law for SHG ($n = 2$), 4HG ($n = 4$), 6HG ($n = 6$), and 8HG ($n = 8$) yield, respectively.

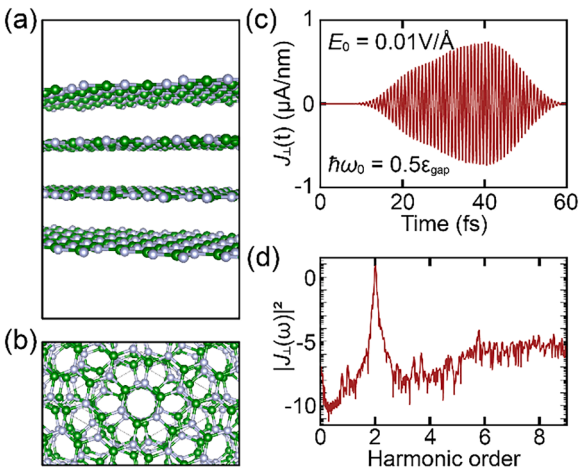

Fig. 7. Observation of SHG in a large multi-layer system. (a) side and (b) top view of twisted 4-layer h-BN. (c) Real-time transverse current density response, and (d) its Fourier transform.

obtained in Fig. 7(d) for twisted 4-layers is consistent with the one shown in Fig. 6(c) for the monolayer under the applied field strength. This can be seen as the combination of the response of each layer to the applied field, whose polarization varies for each layer. A detailed discussion of these effects will be provided in a separate publication. These results validate that our RT-TDDFT implementation in QRCODE with the enhanced OPT-FFT algorithm can give efficient and accurate results for large systems.

4. Conclusion

In conclusion, we have developed a new software module, QRCODE, for massively parallelized velocity-gauge RT-TDDFT calculations of large-scale periodic systems in the open-source Qbox software package. QRCODE utilizes a tailored OPT-FFT algorithm that reduces MPI communication processes by 24% and improves computational performance 1.29 times faster than the traditional FFT algorithm by mapping and padding the band index. In addition to improving computational performance, we have implemented CN and various ETRS time propagators in QRCODE for accurate RT-TDDFT calculations. To demonstrate its computational efficiency, we provide computational benchmarks of QRCODE that show impressive scaling on up to 16,344 CPUs.

To demonstrate the accuracy and applicability of QRCODE, we examined four case studies, including Ehrenfest dynamics of electronic-excited H_2, electronic-excited reaction dynamics of the ozone-oxygen reaction, RT-TDDFT simulations of optical absorption spectra, and nonlinear optical properties of large 2D material systems. The calculation of SHG and HHG signals provides a stringent test of the reliability and accuracy of first-principles material science codes, and our SHG and HHG results for monolayer and twisted multi-layer h-BN sheets agree well with previous studies. We are aware that hybrid functionals are necessary for obtaining more accurate calculations of materials that exhibit self-interaction errors, and future efforts in our group are underway to implement this feature in QRCODE. Taken together, the new massively parallelized routines in QRCODE allow accurate and efficient RT-TDDFT calculations of light-matter interactions, optical response, photocatalysis, and photo-driven reaction dynamics in large-scale, complex material systems.

Data and code availability

The numerical data and the computational source code used to perform the calculations that support our study are available from the corresponding author upon reasonable request.

CRediT authorship contribution statement

Min Choi: Writing – review & editing, Writing – original draft, Visualization, Validation, Software, Methodology, Investigation, Formal analysis, Data curation, Conceptualization. **Mahmut Sait Okyay:** Writing – review & editing, Writing – original draft, Visualization, Validation, Software, Methodology, Investigation, Formal analysis, Data curation, Conceptualization. **Adrian Perez Dieguez:** Writing – review & editing, Writing – original draft, Visualization, Validation, Software, Resources, Methodology, Investigation, Formal analysis, Data curation, Conceptualization. **Mauro Del Ben:** Writing – review & editing, Writing – original draft, Visualization, Validation, Supervision, Software, Resources, Project administration, Methodology, Investigation, Funding acquisition, Formal analysis, Data curation, Conceptualization. **Khaled Z. Ibrahim:** Writing – review & editing, Writing – original draft, Validation, Supervision, Software, Resources, Project administration, Funding acquisition, Formal analysis, Data curation, Conceptualization. **Bryan M. Wong:** Writing – review & editing, Writing – original draft, Supervision, Resources, Project administration, Methodology, Investigation, Funding acquisition, Formal analysis, Conceptualization.

Declaration of competing interest

The authors declare that they have no known competing financial interests or personal relationships that could have appeared to influence the work reported in this paper.

Data availability

Data will be made available on request.

Acknowledgments

This work was supported by the U.S. Department of Energy, Office of Science, Office of Advanced Scientific Computing Research, Scientific Discovery through the Advanced Computing (SciDAC) program under Award Number DE-SC0022209. This research used resources of the National Energy Research Scientific Computing Center (NERSC), a U.S. Department of Energy Office of Science User Facility located at Lawrence Berkeley National Laboratory, operated under Contract No. DE-AC02-05CH11231 using NERSC award BES-ERCAP-m4271.

Supplementary materials

Supplementary material associated with this article can be found, in the online version, at doi:10.1016/j.cpc.2024.109349.

References

[1] G. Petite, Fundamental principles of light-matter interactions, Vide 43 (1988) 333–419.
[2] H.R. Reiss, Fundamental formulation of light-matter interactions revisited, Phys. Rev. A 100 (2019) 052105.
[3] A. Quandt, R. Warmbier, Theory and numerical aspects of fundamental light-matter interactions, J. Opt. Soc. Am. B 37 (2020) A207–A213.
[4] M. Melchionna, P. Fornasiero, Updates on the roadmap for photocatalysis, ACS Catal 10 (2020) 5493–5501.
[5] J. Orenstein, J.E. Moore, T. Morimoto, D.H. Torchinsky, J.W. Harter, D. Hsieh, Topology and symmetry of quantum materials via nonlinear optical responses, Annu. Rev. Condens. Matter Phys. 12 (2021) 247–272.
[6] Q. Ma, A.G. Grushin, K.S. Burch, Topology and geometry under the nonlinear electromagnetic spotlight, Nat. Mater. 20 (2021) 1601–1614.
[7] T. Holder, D. Kaplan, B. Yan, Consequences of time-reversal-symmetry breaking in the light-matter interaction: berry curvature, quantum metric, and diabatic motion, Phys. Rev. Res. 2 (2020) 033100.
[8] D. Shin, S.A. Sato, H. Hübener, U. De Giovannini, J. Kim, N. Park, A. Rubio, Unraveling materials berry curvature and chern numbers from real-time evolution of Bloch states, Proc. Natl. Acad. Sci 116 (2019) 4135–4140.
[9] T. Kitagawa, E. Berg, M. Rudner, E. Demler, Topological characterization of periodically driven quantum systems, Phys. Rev. B 82 (23) (2010) 235114.

[10] J.E. Sipe, A.I. Shkrebtii, Second-order optical response in semiconductors, Phys. Rev. B 61 (2000) 5337–5352.
[11] L. Pan, K.T. Taylor, C.W. Clark, Perturbation theory study of high-harmonic generation, J. Opt. Soc. Am. B 7 (1990) 509–516.
[12] J. Kim, K.-W. Kim, D. Shin, S.-H. Lee, J. Sinova, N. Park, H. Jin, Prediction of ferroelectricity-driven berry curvature enabling charge- and spin-controllable photocurrent in tin telluride monolayers, Nat. Commun. 10 (2019) 3965.
[13] S.-Y. Xu, Q. Ma, H. Shen, V. Fatemi, S. Wu, T.-R. Chang, G. Chang, A.M. M. Valdivia, C.-K. Chan, Q.D. Gibson, J. Zhou, Z. Liu, K. Watanabe, T. Taniguchi, H. Lin, R.J. Cava, L. Fu, N. Gedik, P. Jarillo-Herrero, Electrically switchable berry curvature dipole in the monolayer topological insulator WTe_2, Nat. Phys. 14 (2018) 900–906.
[14] F. de Juan, A.G. Grushin, T. Morimoto, J.E. Moore, Quantized circular photogalvanic effect in Weyl semimetals, Nat. Commun. 8 (2017) 15995.
[15] I. Sodemann, L. Fu, Quantum nonlinear Hall effect induced by berry curvature dipole in time-reversal invariant materials, Phys. Rev. Lett. 115 (2015) 216806.
[16] R.W. Boyd, B. Masters, Nonlinear Optics, 3rd ed., Academic, New York, 2008.
[17] P. Török, F.-J. Kao, Optical Imaging and Microscopy: Techniques and Advanced Systems, 87, Springer, 2007.
[18] Z.-Y. Chen, R. Qin, High harmonic generation in graphene–boron nitride heterostructures, J. Mater. Chem. C 8 (2020) 12085–12091.
[19] H. Liu, Y. Li, Y.S. You, S. Ghimire, T.F. Heinz, D.A. Reis, High-garmonic generation from an atomically thin semiconductor, Nat. Phys. 13 (2017) 262–265.
[20] A.D. Aldabesh, A numerical study of $CsSnI_xBr_{3-x}$ perovskite material as an electron transport layer (ETL), in the perovskite solar cell of a photovoltaic system by molecular dynamics method with LAMMPS software: the effects of external convective heat transfer, Eng. Anal. Bound. Elem. 147 (2023) 51–58.
[21] Q. Chen, X. Wang, P. Yi, P. Zhang, L. Zhang, M. Wu, B. Pan, Key roles of electron cloud density and configuration in the adsorption of sulfonamide antibiotics on carbonaceous materials: molecular dynamics and quantum chemical investigations, Appl. Surf. Sci. 536 (2021) 147757.
[22] M. Guan, S. Hu, H. Zhao, C. Lian, S. Meng, Toward attosecond control of electron dynamics in two-dimensional materials, Appl. Phys. Lett. 116 (2020) 043101.
[23] C. Heide, T. Boolakee, T. Higuchi, P. Hommelhoff, Sub-cycle temporal evolution of light-induced electron dynamics in hexagonal 2D materials, J. Phys.: Photonics 2 (2020) 024004.
[24] X. Tong, M. Bernardi, Toward precise simulations of the coupled ultrafast dynamics of electrons and atomic vibrations in materials, Phys. Rev. Res. 3 (2021) 023072.
[25] J. Mattiat, S. Luber, Comparison of length, velocity, and symmetric gauges for the calculation of absorption and electric circular dichroism spectra with real-time time-dependent density functional theory, J. Chem. Theory Comput. 18 (2022) 5513–5526.
[26] W. Ma, J. Zhang, L. Yan, Y. Jiao, Y. Gao, S. Meng, Recent progresses in real-time local-basis implementation of time dependent density functional theory for electron–nucleus dynamics, Comput. Mater. Sci. 112 (2016) 478–486.
[27] M.E. Casida, M. Huix-Rotllant, Progress in time-dependent density-functional theory, Annu. Rev. Phys. Chem. 63 (2012) 287–323.
[28] A. Castro, H. Appel, M. Oliveira, C.A. Rozzi, X. Andrade, F. Lorenzen, M.A. L. Marques, E.K.U. Gross, A. Rubio, Octopus: a tool for the application of time-dependent density functional theory, *Phys. Status Solidi* (b) 243 (2006) 2465–2488.
[29] A. Bussy, J. Hutter, First-principles correction scheme for linear-response time-dependent density functional theory calculations of core electronic states, J. Chem. Phys. 155 (2021) 034108.
[30] A. Bussy, J. Hutter, Efficient and low-scaling linear-response time-dependent density functional theory implementation for core-level spectroscopy of large and periodic systems, Phys. Chem. Chem. Phys. 23 (2021) 4736–4746.
[31] P. Koval, M. Barbry, D. Sánchez-Portal, PySCF-NAO: an efficient and flexible implementation of linear response time-dependent density functional theory with numerical atomic orbitals, Comput. Phys. Commun. 236 (2019) 188–204.
[32] F. Hofmann, I. Schelter, S. Kümmel, Linear response time-dependent density functional theory without unoccupied states: the Kohn-Sham-Sternheimer scheme revisited, J. Chem. Phys. 149 (2018) 024105.
[33] L. Wan, X. Liu, J. Liu, X. Qin, W. Hu, J. Yang, Hybrid MPI and OpenMP parallel implementation of large-scale linear-response time-dependent density functional theory with plane-wave basis set, Electron. Struct. 3 (2021) 024004.
[34] X. Sheng, H. Zhu, K. Yin, J. Chen, J. Wang, C. Wang, J. Shao, F. Chen, Excited-state absorption by linear response time-dependent density functional theory, J. Phys. Chem. C 124 (2020) 4693–4700.
[35] C.D. Pemmaraju, F.D. Vila, J.J. Kas, S.A. Sato, J.J. Rehr, K. Yabana, D. Prendergast, Velocity-gauge real-time TDDFT within a numerical atomic orbital basis set, Comput. Phys. Commun. 226 (2018) 30–38.
[36] D. Shin, G. Lee, Y. Miyamoto, N. Park, Real-time propagation via time-dependent density functional theory plus the hubbard U potential for electron–atom coupled dynamics involving charge transfer, J. Chem. Theory Comput. 12 (2016) 201–208.
[37] G.F. Bertsch, J.I. Iwata, A. Rubio, K. Yabana, Real-space, real-time method for the dielectric function, Phys. Rev. B 62 (2000) 7998–8002.
[38] L. Ye, H. Wang, Y. Zhang, W. Liu, Self-adaptive real-time time-dependent density functional theory for X-ray absorptions, J. Chem. Phys. 157 (2022) 074106.
[39] T. Trepl, I. Schelter, S. Kummel, Analyzing excitation-energy transfer based on the time-dependent density functional theory in real time, J. Chem. Theory Comput. 18 (2022) 6577–6587.
[40] J. Sun, C.-W. Lee, A. Kononov, A. Schleife, C.A. Ullrich, Real-time exciton dynamics with time-dependent density-functional theory, Phys. Rev. Lett. 127 (2021) 077401.
[41] L. Schreder, S. Luber, Local approaches for electric dipole moments in periodic systems and their application to real-time time-dependent density functional theory, J. Chem. Phys. 155 (2021) 134116.
[42] C. Müller, M. Sharma, M. Sierka, Real-time time-dependent density functional theory using density fitting and the continuous fast multipole method, J. Comput. Chem. 41 (2020) 2573–2582.
[43] T. Moitra, L. Konecny, M. Kadek, A. Rubio, M. Repisky, Accurate relativistic real-time time-dependent density functional theory for valence and core attosecond transient absorption spectroscopy, J. Phys. Chem. Lett. 14 (2023) 1714–1724.
[44] A. Kononov, C.-W. Lee, T.P. dos Santos, B. Robinson, Y. Yao, Y. Yao, X. Andrade, A. D. Baczewski, E. Constantinescu, A.A. Correa, Y. Kanai, N. Modine, A. Schleife, Electron dynamics in extended systems within real-time time-dependent density-functional theory, MRS Commun. 12 (2022) 1002–1014.
[45] J. Hekele, Y. Yao, Y. Kanai, V. Blum, P. Kratzer, All-electron real-time and imaginary-time time-dependent density functional theory within a numeric atom-centered basis function framework, J. Chem. Phys. 155 (2021) 154801.
[46] S. Meng, E. Kaxiras, Real-time, local basis-set implementation of time-dependent density functional theory for excited state dynamics simulations, J. Chem. Phys. 129 (2008) 054110.
[47] J. Ren, E. Kaxiras, S. Meng, Optical properties of clusters and molecules from real-time time-dependent density functional theory using a self-consistent field, Mol. Phys. 108 (14) (2010) 1829–1844.
[48] C. Lian, M. Guan, S. Hu, J. Zhang, S. Meng, Photoexcitation in solids: first-principles quantum simulations by real-time TDDFT, Adv. Theory Simul. 1 (2018) 1800055.
[49] Y. Takimoto, F.D. Vila, J.J. Rehr, Real-time time-dependent density functional theory approach for frequency-dependent nonlinear optical response in photonic molecules, J. Chem. Phys. 127 (2007) 154114.
[50] X. Andrade, C.D. Pemmaraju, A. Kartsev, J. Xiao, A. Lindenberg, S. Rajpurohit, L. Z. Tan, T. Ogitsu, A.A. Correa, INQ, a modern GPU-accelerated computational framework for (time-dependent) density functional theory, J. Chem. Theory Comput. 17 (2021) 7447–7467.
[51] M. Noda, S.A. Sato, Y. Hirokawa, M. Uemoto, T. Takeuchi, S. Yamada, A. Yamada, Y. Shinohara, M. Yamaguchi, K. Iida, I. Floss, T. Otobe, K.-M. Lee, K. Ishimura, T. Boku, G.F. Bertsch, K. Nobusada, K.S. Yabana, Scalable Ab-initio light–matter simulator for optics and nanoscience, Comput. Phys. Commun 235 (2019) 356–365.
[52] The Elk Code. http://elk.sourceforge.net.
[53] N. Tancogne-Dejean, M.J.T. Oliveira, X. Andrade, H. Appel, C.H. Borca, G. Le Breton, F. Buchholz, A. Castro, S. Corni, A.A. Correa, U. De Giovannini, A. Delgado, F.G. Eich, J. Flick, G. Gil, A. Gomez, N. Helbig, H. Hübener, R. Jestädt, J. Jornet-Somoza, A.H. Larsen, I.V. Lebedeva, M. Lüders, M.A.L. Marques, S.T. Ohlmann, S. Pipolo, M. Rampp, C.A. Rozzi, D.A. Strubbe, S.A. Sato, C. Schäfer, I. Theophilou, A. Welden, A. Rubio, Octopus, a computational framework for exploring light-driven phenomena and quantum dynamics in extended and finite systems, J. Chem. Phys. 152 (2020) 124119.
[54] X. Andrade, D.A. Strubbe, U. De Giovannini, A.H. Larsen, M.J.T. Oliveira, J. Alberdi-Rodriguez, A. Varas, I. Theophilou, N. Helbig, M. Verstraete, L. Stella, F. Nogueira, A. Aspuru-Guzik, A. Castro, M.A.L. Marques, A. Rubio, Real-space grids and the octopus code as tools for the development of new simulation approaches for electronic systems, Phys. Chem. Chem. Phys. 17 (2015) 31371–31396.
[55] A. Castro, H. Appel, M. Oliveira, C.A. Rozzi, X. Andrade, F. Lorenzen, M.A. L. Marques, E.K.U. Gross, A. Rubio, Octopus: a tool for the application of time-dependent density functional theory, Phys. Stat. Sol. B 243 (2006) 2465–2488.
[56] M.A.L. Marques, A. Castro, G.F. Bertsch, A. Rubio, Octopus: a first-principles tool for excited electron-ion Dynamics, Comput. Phys. Commun. 151 (2003) 60–78.
[57] P. Raizada, V. Soni, A. Kumar, P. Singh, A.A.P. Khan, A.M. Asiri, V.K. Thakur, V. H. Nguyen, Surface defect engineering of metal oxides photocatalyst for energy application and water treatment, J. Materiom. 7 (2021) 388–418.
[58] Z.L. Wang, M. Xiao, J.K. You, G. Liu, L.Z. Wang, Defect engineering in photocatalysts and photoelectrodes: from small to big, Acc. Mater. Res. 3 (2022) 1127–1136.
[59] S. Chaudhary, C. Knapp, G. Refael, Anomalous exciton transport in response to a uniform in-plane electric field, Phys. Rev. B 103 (2021) 165119.
[60] Y. Jiang, S.L. Chen, W.H. Zheng, B.Y. Zheng, A.L. Pan, Interlayer exciton formation, relaxation, and transport in TMD van der Waals heterostructures, Light Sci. Appl. 10 (2021) 72.
[61] F. Gygi, Architecture of Qbox: a scalable first-principles molecular dynamics code, IBM J. Res. Dev. 52 (2008) 137–144.
[62] F. Gygi, I. Duchemin, D. Donadio, G. Galli, Practical algorithms to facilitate large-scale first-principles molecular dynamics, J. Phys.: Conf. Ser. 180 (2009) 012074.
[63] F. Gygi, R.K. Yates, J. Lorenz, E.W. Draeger, F. Franchetti, C.W. Ueberhuber, B.R. d. Supinski, S. Kral, J.A. Gunnels, J.C. Sexton, Large-scale first-principles molecular dynamics simulations on the BlueGene/L platform using the Qbox code, in: SC '05: Proceedings of the 2005 ACM/IEEE Conference on Supercomputing, Seattle, WA, USA, 2005, p. 2.
[64] F. Gygi, E.W. Draeger, M. Schulz, B.R.d Supinski, J.A. Gunnels, V. Austel, J. C. Sexton, F. Franchetti, S. Kral, C.W. Ueberhuber, J. Lorenz, Large-scale electronic structure calculations of high-Z metals on the BlueGene/L platform, in: SC '06: Proceedings of the 2006 ACM/IEEE conference on Supercomputing, Tampa, FL, USA, 2006, p. 45.
[65] A. Schleife, E.W. Draeger, Y. Kanai, A.A. Correa, Plane-wave pseudopotential implementation of explicit integrators for time-dependent Kohn-Sham equations in large-scale simulations, J. Chem. Phys. 137 (2012) 22A546.

[66] A. Schleife, E.W. Draeger, V.M. Anisimov, A.A. Correa, Y. Kanai, Quantum dynamics simulation of electrons in materials on high-performance computers, Comput. Sci. Eng. 16 (2014) 54–60.
[67] E.W. Draeger, X. Andrade, J.A. Gunnels, A. Bhatele, A. Schleife, A.A. Correa, Massively parallel first-principles simulation of electron dynamics in materials, J. Parallel Distrib. Comput. 106 (2017) 205–214.
[68] A. Castro, M.A.L. Marques, A. Rubio, Propagators for the time-dependent Kohn-Sham equations, J. Chem. Phys. 121 (2004) 3425–3433.
[69] J. Crank, P. Nicolson, A practical method for numerical evaluation of solutions of partial differential equations of the heat-conduction type, Adv. Comput. Math. 6 (1996) 207–226.
[70] D.R. Fokkema, G.L.G. Sleijpen, H.A. VanderVorst, Generalized conjugate gradient squared, J. Comput. Appl. Math. 71 (1996) 125–146.
[71] Y. Miyamoto, H. Zheng, Testing the numerical stability of time-dependent density functional simulations using the Suzuki-Trotter formula, Phys. Rev. B 77 (2008) 165123.
[72] R.W. Boyd, Nonlinear Optics, Third ed., Academic Press, 2008.
[73] F. Simon, S. Clevers, V. Dupray, G. Coquerel, Relevance of the second harmonic generation to characterize crystalline samples, Chem. Eng. Technol. 38 (2015) 971–983.
[74] Z.Y. Chen, R. Qin, Circularly polarized extreme ultraviolet high harmonic generation in graphene, Opt. Express 27 (2019) 3761–3770.
[75] Y.S. You, D.A. Reis, S. Ghimire, Anisotropic high-harmonic generation in bulk crystals, Nat. Phys. 13 (2017) 345–349.
[76] NERSC documentation: https://docs.nersc.gov/systems/perlmutter/.
[77] Cray LibSci. HPE Cray. https://cpe.ext.hpe.com/docs/csml/cray_libsci.html.
[78] L.S. Blackford, et al., An updated set of basic linear algebra subprograms (BLAS), ACM Transact. Math. Softw. 28 (2002) 135–151.
[79] E. Anderson, et al., LAPACK Users Guide, Society for Industrial and Applied Mathematics, Philadelphia, PA, 1999.
[80] The Apache XML project. Apache. https://xerces.apache.org/xerces-c/ (last accessed: July 17, 2024).
[81] J.P. Perdew, K. Burke, M. Ernzerhof, Generalized gradient approximation made simple, Phys. Rev. Lett. 77 (1996) 3865.
[82] P.W. Atkins, General Chemistry, Freeman & Company, W&H, New York, 1989, p. 989.
[83] S. Chung, C.C. Lin, E.T.P. Lee, Dissociation of hydrogen molecule by electron-impact, Phys. Rev. A 12 (1975) 1340–1349.
[84] H.U. Dütsch, The photochemistry of stratospheric ozone, Q. J. R. Meteorol. Soc. 94 (1968) 483–497.
[85] D.R. Hamann, Optimized norm-conserving vanderbilt pseudopotentials, Phys. Rev. B 88 (2013) 085117.
[86] M.S. Okyay, S.A. Sato, K.W. Kim, B.H. Yan, H. Jin, N. Park, Second harmonic Hall responses of insulators as a probe of berry curvature dipole, Commun. Phys. 5 (2022) 303.
[87] R. Sinha-Roy, P. Garcia-Gonzalez, X.L. Lozano, R.L. Whetten, H.C. Weissker, Identifying electronic modes by Fourier transform from delta-kick time-evolution TDDFT calculations, J. Chem. Theory. Comput. 14 (2018) 6417–6426.
[88] L. Chen, C. Xiong, J. Xiao, H.C. Yuan, A time-asymmetric delta-kicked model for the quantum Ratchet effect, Physica A 416 (2014) 225–230.
[89] C. Elias, P. Valvin, T. Pelini, A. Summerfield, C.J. Mellor, T.S. Cheng, L. Eaves, C. T. Foxon, P.H. Beton, S.V. Novikov, B. Gil, G. Cassabois, Direct band-gap crossover in epitaxial monolayer boron nitride, Nat. Commun 10 (2019) 2639.
[90] C.G. Henriques, G.B. Ventura, C.D.M. Fernandes, N.M.R Peres, Optical absorption of single-layer hexagonal boron nitride in the ultraviolet, J. Phys.: Condens. Matter 32 (2020) 025304.
[91] C.D. Pemmaraju, Simulation of attosecond transient soft X-ray absorption in solids using generalized Kohn-Sham real-time time-dependent density functional theory, New J. Phys. 22 (2020) 083063.
[92] S.K. Kurtz, T.T. Perry, A powder technique for the evaluation of nonlinear optical materials, J. Appl. Phys. 39 (1968) 3798–3813.
[93] J.P. Dougherty, S.K. Kurtz, A second harmonic analyzer for the detection of non-centrosymmetry, J. Appl. Crystallogr. 9 (1976) 145–158.
[94] Z.Y. Chen, R. Qin, High harmonic generation in graphene-boron nitride heterostructures, J. Mater. Chem. C 8 (2020) 12085–12091.
[95] H.Z. Liu, Y.L. Li, Y.S. You, S. Ghimire, T.F. Heinz, D.A. Reis, High-harmonic generation from an atomically thin semiconductor, Nat. Phys. 13 (2017) 262–265.
[96] H. Wang, X.F. Qian, Giant optical second harmonic generation in two-dimensional multiferroics, Nano Lett 17 (2017) 5027–5034.
[97] T.T. Luu, H.J. Worner, Measurement of the berry curvature of solids using high-harmonic spectroscopy, Nat. Commun. 9 (2018) 916.
[98] J.W. Sun, A. Ruzsinszky, J.P. Perdew, Strongly constrained and appropriately normed semilocal density functional, Phys. Rev. Lett. 115 (2015) 036402.